Dynamical approach to the spatiotemporal aspects of the Portevin–Le Chatelier effect: Chaos, turbulence, and band propagation

G. Ananthakrishna[1,2] and M. S. Bharathi[1]
[1]*Materials Research Centre, Indian Institute of Science, Bangalore-560012, India*
[2]*Centre for Condensed Matter Theory, Indian Institute of Science, Bangalore-560012, India*
(Received 10 December 2003; published 25 August 2004)

The analysis of experimental time series, obtained from single and polycrystals subjected to constant strain rate tests, reports an intriguing dynamical crossover from a low-dimensional chaotic state at medium strain rates to an infinite-dimensional power-law state of stress drops at high strain rates. We present the results of an extensive study of all aspects of the Portevin–Le Chatelier (PLC) effect within the context of a recent model that reproduces this crossover. We characterize the dynamics of this crossover by studying the distribution of the Lyapunov exponents as a function of the strain rate, with special attention to system size effects. The distribution of the exponents changes from a small set of positive exponents in the chaotic regime to a dense set of null exponents in the scaling regime. As the latter is similar to the result in a shell model for turbulence, we compare the results of our model with that of the shell model. Interestingly, the null exponents in our model themselves obey a power law. The study is complimented by visualizing the configuration of dislocations through the slow manifold analysis. This shows that while a large proportion of dislocations are in the pinned state in the chaotic regime, most of them are pushed to the threshold of unpinning in the scaling regime, thus providing insight into the mechanism of crossover. We also show that this model qualitatively reproduces the different types of deformation bands seen in experiments. At high strain rates, where propagating bands are seen, the model equations can be reduced to the Fisher-Kolmogorov equation for propagative fronts, which in turn shows that the velocity of the propagation of the bands varies linearly with the strain rate and inversely with the dislocation density. These results are consistent with the known experimental results. We also discuss the connection between the nature of band types and the dynamics in the respective regimes. The analysis demonstrates that this simple dynamical model captures the complex spatiotemporal features of the PLC effect.

DOI: 10.1103/PhysRevE.70.026111 PACS number(s): 62.20.Mk, 05.65.+b, 05.45.Ac, 62.20.Fe

I. INTRODUCTION

Plastic deformation is a highly dissipative irreversible nonequilibrium process where nonlinearities play a fundamental role. Under normal conditions, one finds homogeneous deformation. However, under suitable conditions of deformation, different types of spatial and temporal patterns are observed that can be broadly classified by the associated time and length scales—for example, the persistent slip bands lasting over long time scales [1,3] and the propagative Lüders bands characterized by short time scales [1,3]. Yet another and even more complex spatitemporal pattern is observed during tension tests of dilute metallic alloys in a certain range of strain rates and temperatures. This phenomenon has come to be known as the Portevin–Le Chatelier (PLC) effect [2]. Here a uniform deformation mode becomes unstable, leading to a spatially and temporally inhomogeneous state. The instability manifests itself in the form of serrations on the stress-strain curves of the sample [1,3]. Each stress drop is generally associated with the nucleation and often the propagation of a band of localized plastic deformation. In polycrystals, these bands and the associated serrations are classified into three generic types. On increasing the strain rate or decreasing the temperature, one first finds the type *C* band, identified with randomly nucleated static bands with large characteristic stress drops on the stress-strain curve. The serrations are quite regular. Then the type *B* "hopping" bands are seen. The serrations are more irregular with amplitudes that are smaller than that for the type *C*. The bands that are formed are still localized and static in nature, but they form ahead of the previous band in a spatially correlated way, giving the visual impression of a hopping propagation. Finally, one observes the continuously propagating type *A* bands associated with small stress drops. (In single crystals, such a clear classification does not exist.) These different types of PLC bands are believed to represent distinct correlated states of dislocations in the bands.

The well-accepted classical explanation of the PLC effect is via the dynamic strain aging concept introduced by Cottrell [4] and later extended by others [1,5–7]. (An alternate approach to the study of collective effects of dislocations is due to Weertman [8], who uses the Bilby-Cottrell-Swindsen crack problem.) In Cottrell's picture, the dynamic strain aging refers to the interaction of mobile dislocations with the diffusing solute atoms. At low strain rates (or high temperatures) the average velocity of dislocations is low and there is sufficient time for the solute atoms to diffuse to the dislocations and pin them (called "aging"). Thus, the longer the dislocations are arrested, the larger will be the stress required to unpin them. When these dislocations are unpinned, they move at large speeds until they are arrested again. At high strain rates (or low temperatures), the time available for solute atoms to diffuse to the dislocations decreases and hence the stress required to unpin them decreases. Thus, in a range of strain rates and temperatures, where these two time scales are of the same order of magnitude, the PLC instability

manifests. The competition between the slow rate of pinning and the sudden unpinning of the dislocations, at the macroscopic level, translates into a negative strain rate sensitivity of the flow stress as a function of strain rate, which is the basic instability mechanism used in most phenomenological models [1,3]. Slow-fast dynamics and the negative flow-rate characteristic are common to many stick-slip systems, such as frictional sliding [9], fault dynamics [10], peeling of an adhesive tape [11], and charge-density waves [12].

There are two different types of challenges in dealing with the PLC effect. The first is understanding the collective behavior of dislocations, which has been slow, largely due to the lack of techniques for describing the cooperative behavior of dislocations. Second, the PLC effect involves collective modes of dislocations, where both fast and slow times scales play an equally important role, requiring specific techniques of nonlinear dynamics. Further, these time scales themselves evolve as a function of strain rate and temperature, which in turn leads to different types of serrations. At a low strain rate, the existence of both fast (time scales over which stress drops occur) and slow time scales (loading time scales) are clearly displayed in the stress-strain curves. However, at a high strain rate, as internal (plastic) relaxation is not complete, a clear demarcation of time scales is difficult. This, along with the corresponding length scales (bandwidths), points to extremely complex underlying dynamics.

The inherent nonlinearity and presence of multiple time scales necessitates the use of techniques of nonlinear dynamics for a proper understanding of this phenomenon. The first dynamical approach was undertaken in the early 1980s by Ananthakrishna and co-workers [13], which affords a natural basis for the description of the time-dependent aspects of the PLC effect. It also allows for the explicit inclusion and interplay of different time scales inherent in the dynamics of dislocations. The original model attempts to address the time dependence of the phenomenon using three types of dislocation densities assumed to represent the collective degrees of freedom of dislocations [13]. Despite the simplicity of the model, many generic features of the PLC effect, such as the existence of a window of strain rates and temperatures within which it occurs, etc., were correctly reproduced. More importantly, the *negative strain rate sensitivity was shown to emerge naturally* in the model, as a result of nonlinear interaction of the participating defects [13,14].

Due to the dynamical nature of the model, one prediction is the existence of the chaotic stress drops in a certain range of temperatures and strain rates [15], subsequently verified by analyzing the stress-time series [16,17] using dynamical methods [18,19]. The number of degrees of freedom estimated from such an analysis of experimental time series turn out to be the same as in the model offering justification for ignoring spatial degrees of freedom. These studies have also shown that a wealth of dynamical information can be extracted from the stress-time series [16,17]. Further efforts showed the existence of *an intriguing crossover from a chaotic state at low and medium strain rates to a power-law state of stress drops at high strain rates* [20,21]. As the crossover is observed in both single and polycrystals, it appears to be insensitive to the microstructure. However, the chaotic state is dynamically a distinct state from the power-law state, as the former involves a small number of degrees of freedom characterized by the self-similarity of the attractor and sensitivity to initial conditions [19], while the latter is an infinite-dimensional state reminiscent of self-organized criticality (SOC) [22–24]. Due to this basic difference in the nature of the dynamics, most systems exhibit either of these states. More importantly, these studies also demonstrate that the chaotic state at intermediate strain rates is correlated with the type *B* band and the power-law regime of stress drops at high strain rates with the propagating type *A* band [21]. These authors also make a connection between the transition in the nature of serration between the type *B* and A bands' regime of strain rates with the Anderson's transition in condensed matter physics. Thus, it appears that the PLC effect is a storehouse of many paradigms in condensed matter physics. Indeed, recently, the spatiotemporal features of the PLC effect have also attracted attention from physicists [25]. Understanding these connections between the dynamics and general features of the PLC effect would give insight into the rich physics.

The dynamics of the crossover as a function of strain rate is *unusual in a number of ways*. First, the PLC effect is one of the two rare instances where such an intriguing crossover phenomenon is seen, the other being in the hydrodynamic turbulence [26]. Second, the power law, both in the PLC effect and turbulence, arises at high drive rates [26,27]. Thus, it would be interesting to examine the similarity and differences with hydrodynamic turbulence by comparing, the results of the Lyapunov spectrum of our PLC model with that of the Gledzer-Ohkitani-Yamada shell model of turbulence. (Henceforth, we refer to this model as shell model for brevity [27,28].) Further, such a study helps us to compare the nature of the Lyapunov spectrum with the conventional SOC systems seen at low drives (such as those in earthquakes [29] and Barkhausen noise [30]). For lack of anything better, we shall reserve SOC for power-law situations at low drives. Finally, as different types of bands are a characteristic feature of the PLC effect, we investigate the connection between spatial aspects and the nature of the dynamics.

The fully dynamical nature of the Ananthakrishna's model makes it most suitable for studying this crossover by including spatial degrees of freedom. We report a detailed investigation of all these issues (reported in brief earlier [31,32]). Particular attention will be paid to study the system size effects during the crossover.

Section II introduces the dynamical model and its extension to include spatial degrees of freedom. Section III contains the numerical procedure used. In Sec. IV, we introduce the background material used for the study. Section V contains a comparison of the results of the analysis of experimental time series with that of the model. Section VI contains all the major results on the dynamics of crossover, including the evolution of the Lyapunov spectrum as a function of the strain rate and the analysis of the distribution of null exponents in the power-law regime of stress drops. Section VI also includes a comparison of the results of the model with that of the shell model for turbulence, followed by the slow manifold method of visualization of dislocation configurations. Finally, in Sec. VII we discuss both analytical and numerical results on the nature of dislocation bands. We

conclude the paper with a few general comments.

II. THE ANANTHAKRISHNA'S MODEL

In the model [13], the well-separated time scales subsumed in the dynamic strain aging concept are mimicked by three types of dislocations, namely, the fast mobile, immobile, and "decorated" Cottrell-type dislocations. As the model has been studied in detail by our group [13,14,34,33] (see also [35,36]), following the notation in Ref. [14], we shall briefly outline the model in scaled variables. The evolution equations for the densities of the mobile, immobile, and Cottrell-type dislocations denoted by $\rho_m(x,t)$, $\rho_{im}(x,t)$, and $\rho_c(x,t)$, respectively are

$$\frac{\partial \rho_m}{\partial t} = -b_0\rho_m^2 - \rho_m\rho_{im} + \rho_{im} - a\rho_m + \phi_{eff}^m\rho_m + \frac{D}{\rho_{im}}\frac{\partial^2(\phi_{eff}^m(x)\rho_m)}{\partial x^2}, \tag{1}$$

$$\frac{\partial \rho_{im}}{\partial t} = b_0(b_0\rho_m^2 - \rho_m\rho_{im} - \rho_{im} + a\rho_c), \tag{2}$$

$$\frac{\partial \rho_c}{\partial t} = c(\rho_m - \rho_c). \tag{3}$$

The model includes the following dislocation mechanisms: immobilization of two mobile dislocations due to the formation of locks ($b_0\rho_m^2$), the annihilation of a mobile dislocation with an immobile one ($\rho_m\rho_{im}$), and the remobilization of the immobile dislocation due to stress or thermal activation (ρ_{im}). It also includes the immobilization of mobile dislocations due to solute atoms ($a\rho_m$). Once a mobile dislocation starts acquiring solute atoms we regard it as the Cottrell-type dislocation ρ_c. As they progressively acquire more solute atoms, they eventually stop, and are considered immobile dislocations ρ_{im}. Alternately, the aggregation of solute atoms can be regarded as the definition of ρ_c, i.e., $\rho_c = \int_{-\infty}^{t} dt' \rho_m(t')K(t-t')$, where $K(t)$ is an appropriate kernel. For the sake of simplicity, this kernel is modeled through a single time scale, $K(t)=e^{-ct}$. The convoluted nature of the integral physically implies that the mobile dislocations to which solute atoms aggregate earlier will be aged more than those which acquire solute atoms later (see Ref. [14]). The fifth term in Eq. (1) represents the rate of multiplication of dislocations due to cross slip. This depends on the velocity of the mobile dislocations taken to be $V_m(\phi)=\phi_{eff}^m$, where $\phi_{eff}=(\phi-h\rho_{im}^{1/2})$ is the scaled effective stress, ϕ the scaled stress, m the velocity exponent, and h a work-hardening parameter.

The nature of the spatial coupling in the PLC effect has been a matter of much debate [1]. Several mechanisms have been suggested as a source of spatial coupling, such as compatibility stresses between the slipped and the unslipped regions, long-range interactions, and triaxiality of stresses [1]. Within the scope of our model, cross slip is a natural source of spatial coupling, as dislocations generated due to cross slip at a point spread over to the neighboring elements. Let Δx be an elementary length. Then, the rate of production of dislocations $\Phi(x)=V_m(x,t)\rho_m(x,t)$, at a point x spreading into $x\pm\Delta x$ and vice versa, is given by

$$\Phi(x) + \frac{p}{2}[\Phi(x+\Delta x) - 2\Phi(x) + \Phi(x-\Delta x)], \tag{4}$$

where p is the probability of cross slip spreading into neighboring elements. Expanding $\Phi(x\pm\Delta x)$ and keeping the leading terms, we get

$$\rho_m V_m + \frac{p}{2}\frac{\partial^2(\rho_m V_m)}{\partial x^2}(\Delta x)^2. \tag{5}$$

We further note that cross slip spreads only into regions of minimum back stress. It is well known that considerable contribution to the back stress arises from the existing immobile dislocation density ahead of it. The length scale over which the effect of the back stress is felt is conventionally taken to be proportional to $\rho_{im}^{-1/2}$. As Δx is a measure of the distance over which a dislocation produced at x spreads into the neighboring element, Δx can be identified with the back stress length scale. In addition, to account for all the allowed dislocation configurations, we use an ensemble averaged value of Δx^2, i.e., $\Delta x^2=\langle\Delta x^2\rangle=\overline{r^2}\rho_{im}^{-1}$, where $\langle\ldots\rangle$ refers to the ensemble average and $\overline{r^2}$ is an elementary (dimensionless) length. Using this, we have $D=p\overline{r^2}/2$. (Note that in scaled form $V_m\rho_m=\phi^m\rho_m$.) Finally, a, b_0, and c are the scaled rate constants referring, respectively, to the concentration of solute atoms slowing down the mobile dislocations, the thermal and athermal reactivation of immobile dislocations, and the rate at which the solute atoms are gathering around the mobile dislocations. We note here that the order of magnitudes of the constants have been identified in Refs. [13,33,36]. These equations are coupled to the machine equation

$$\frac{d\phi(t)}{dt} = d\left[\dot{\epsilon} - \frac{1}{l}\int_0^l \rho_m(x,t)\phi_{eff}^m(x,t)dx\right], \tag{6}$$

where $\dot{\epsilon}$ is the scaled applied strain rate, d the scaled effective modulus of the machine and the sample, and l the dimensionless length of the sample. (We reserve $\dot{\epsilon}_a$ for the unscaled strain rate.) Actually, many of these rate constants [the first, second, third, and fourth terms in Eq. (1)] are functions of the velocity of mobile dislocation that we have ignored for the sake of simplicity, particularly as this affects only the domain of instability without affecting other features [37]. Note the feedback mechanism between Eqs. (6) and (1), wherein the former determines the stress which itself depends on the difference between the applied strain rate and the average plastic strain rate. This in turn determines the dislocation multiplication in Eq. (1). This type of global coupling [Eq. (6)] is common to many other situations, for instance, in the nonlinear transport properties of charge-density waves (in blue bronze for example) [12]. We shall make some comments on this later.

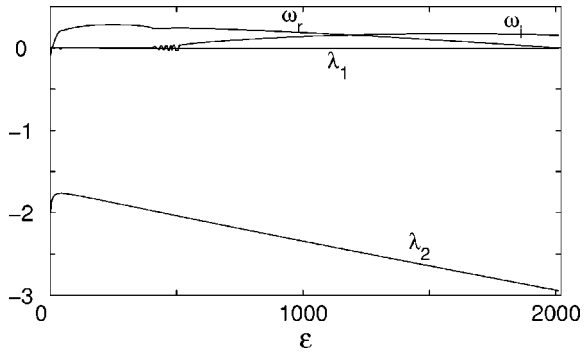

FIG. 1. Eigenvalue spectrum of the fixed point for the model. ω_r and ω_i refer to the real and imaginary parts of the eigenvalue.

III. NUMERICAL SOLUTION OF THE MODEL

We first note that the spatial dependence of ρ_{im} and ρ_c arises only through that of ρ_m. We solve the above set of equations by discretizing the specimen length into N equal parts. Then, $\rho_m(j,t)$, $\rho_{im}(j,t)$, $\rho_c(j,t)$, $j=1,\ldots,N$, and $\phi(t)$ are solved. The widely differing time scales [14,31,34] calls for appropriate care in the numerical solutions. We use a variable step, fourth-order Runge-Kutta scheme with an accuracy of 10^{-6} for all four variables. The spatial derivative in ρ_m is approximated by its central difference. The initial values of the dislocation densities are so chosen that they mimic the values in real samples. They are uniformly distributed with a Gaussian spread along the sample. However, for most calculations, we have used the steady-state values for the variables, as the long term evolution does not depend on the initial values. As for the boundary conditions, we note that the sample is strained at the grips. This means that there is a high density of immobile dislocations at the ends of the sample. We simulate this by employing 2 orders of magnitude higher values for $\rho_{im}(j,t)$ at the end points $j=1$, and N than the rest of the sample. Further, as bands cannot propagate into the grips, we use $\rho_m(j,t)=\rho_c(j,t)=0$ at $j=1$ and N.

As in the original model ($D=0$), as a function of the applied strain rate, the PLC state is reached through a Hopf bifurcation (the lower critical strain $\dot{\epsilon}_{c_1}\sim 35$) and is terminated by a reverse Hopf bifurcation ($\dot{\epsilon}_{c_2}\sim 1000$) when the other parameters are kept in the instability domain. Thus, the instability domain increases substantially compared to the case when $D=0$, due to fact that the instability range depends on the value of D due to the global coupling in Eq. (6). (The domain converges quickly as a function of N.) The number of complex conjugate roots are $2N$, the negative ones are N and one zero exponent. A set of four eigenvalues are shown in Fig. 1 for $a=0.8$, $b_0=0.0005$, $c=0.08$, $d=0.00006$, $m=3.0$, and $h=0$ with $D=0.5$. Beyond $\dot{\epsilon}_{c_2}\sim 1000$ a uniform steady state exits. Although the numerical results reported in the present work are for the above values, the results hold true for a wide range of values of other parameters in the instability domain, including a range of values of D. Various system sizes are used depending upon the property studied, but are generally in the range $N=100-3333$. A sequence of values of N are used wherever convergence of the properties are investigated.

IV. METHODOLOGY

As our approach is fully dynamical and keep in view the materials science community, we collect here a few definitions and provide some details of the methodology used in the analysis. Characterizing the dynamics of the model equations is carried out by studying the Lyapunov spectrum. The number of Lyapunov exponents M for a given N is $M=3N+1$. We shall also use two other well-known invariants, namely the Kaplan-Yorke dimension $D_{KY}=j+\Sigma_{i=1}^{j}\lambda_i/|\lambda_{j+1}|$, where j is such that $\Sigma_{i=1}^{j}\lambda_i>0, \Sigma_{i=1}^{j+1}\lambda_i<0$ and the Kolmogorov entropy $H=\Sigma_{i=1}^{p}\lambda_i$, such that $\lambda_p\geqslant 0$ and $\lambda_{p+1}<0$. One important issue relevant to systems with many degrees of freedom is the existence of a limiting density for the Lyapunov spectrum as the system size is increased. This requires that we should ascertain if λ_j vs $x=j/L^d$ converges to a well-defined asymptotic density function $\Lambda(x)$ with $x\in[0,1]$. (See Ref. [27].) We address this issue by calculating the spectrum for various system sizes $N=100-3333$, which covers approximately 2 orders in M. In particular, such a study will be useful in comparing the results of our model with the shell model for turbulence [28] in the power-law regime of stress drops. Then, one expects that j/D_{KY} converges to a well-defined density function. Following Ref. [28], we use j/D_{KY} vs an appropriately scaled quantity $\lambda_j D_{KY}/H$. This quantity is expected to converge to $f(\lambda_j D_{KY}/H)$. (We note here that the distribution function is proportional to the negative derivative of f.) The nature of the converged Lyapunov density function $f(\lambda_j D_{KY}/H)$ as a function of the drive parameter $\dot{\epsilon}$ can be used to quantify the changes in the dynamics during the crossover.

As stated earlier, a proper description of the PLC effect requires a method of dealing with both the slow and fast time scales, which in turn requires special techniques in nonlinear dynamics. In the model equations, Eq. (1) represents fast dynamics compared to the rest. Both Eqs. (2) and (6) are slow, while (3) falls in between. Such a system can be studied by eliminating the fast variable, thereby allowing a reduction in the dimensionality of the system [38]. To illustrate this, consider

$$\mu\dot{x} = f(x,y,\mu), \tag{7}$$

$$\dot{y} = g(x,y,\mu), \tag{8}$$

where μ is a small parameter and $x\in\mathbb{R}^p$ and $y\in\mathbb{R}^q$. The main feature of such systems is that x evolves much faster than y unless $f(x,y,\mu)$ is small. In the vicinity of the slow manifold defined by $f(x,y,\mu)=0$, the dynamics is characterized by the evolution of the slow variable y. Thus, there is a reduction in the dimensionality of the system. On the other hand, if one is interested in the fast subsystem, using a scaled time $\tau=t/\mu$, we get the corresponding fast variable x defined by Eq. (7), where the slow variables y act as parameters [obtained from Eq. (8)]. This subspace is clearly the complimentary subspace of the slow manifold. We shall use these two subspaces for the visualization of dislocation configurations in the high strain rate power-law regime and obtain the band velocity at high strain rates, respectively.

The analysis of the experimental stress-time series is carried out by estimating both the correlation dimension ν and the Lyapunov spectrum. These methods involve embedding the scalar time series in a higher dimensional space using time-delay techniques [19,39]. Given a time series $\{\sigma_j | j=1,..,P\}$, one first constructs vectors $\vec{\xi}_i = (\sigma_i, \sigma_{i-\tau}, \sigma_{i-2\tau}, \ldots, \sigma_{P-(d-1)\tau})$ in a d-dimensional space. The assumption here is that the actual dynamics can be unfolded by embedding the time series in a higher dimensional space in which the original attractor resides. (In addition, surrogate data analysis was also carried out in [20].) Then, a quantitative estimate of the self-similarity of the attractor, namely the correlation dimension ν, can be obtained by calculating the integral [40] $C(r) = (1/N_T)\Sigma\Theta(r - |\vec{\xi}_i - \vec{\xi}_j|) \sim r^{\nu}$, where N_T is the total number of points in the sum. Correlation dimension also provides a lower bound for the number of degrees of freedom required for a dynamical description of the system, which is given by the minimum integer larger than $\nu+1$ [41]. The geometrical interpretation of these degrees of freedom is that they correspond to the subspace to which the trajectories are confined. The dimension of this subspace can be obtained directly by using singular value decomposition [42]. This method is often used for filtering noise components superposed on the time series. However, in the present context, the method can be used for the *visualization of the strange attractor*. (This method has been applied to the PLC time series earlier [17].) The method involves setting up the $m \times d$ trajectory matrix $\mathbf{T}$ defined by $(\vec{\xi}_1, \vec{\xi}_2, \ldots, \vec{\xi}_m)$, where $m = P - (d-1) \times \tau$. The eigenvalues of the matrix are obtained using the standard method of decomposition $\mathbf{T} = \mathbf{U}\mathbf{W}\mathbf{V}^{\mathbf{T}}$, where $\mathbf{U}$ is $m \times d$ orthogonal matrix, $\mathbf{V}$ is a $d \times d$ unitary matrix, and $\mathbf{W}$ is the matrix of eigenvalues of the covariance matrix of $\mathbf{T}$, which are all nonnegative. The eigenvalues usually decrease rapidly, saturating to a level below which the changes are minimal. Then, the dimension of the attractor is taken to be that corresponding to a number at which the eigenvalues saturate.

V. COMPARISON WITH EXPERIMENTS

To motivate, we begin by briefly recalling the relevant experimental results on the crossover phenomenon and then comparing them with those from the model. We begin by comparing the nature of serrations in the respective regimes of strain rate. Figures 2(a) and 2(b) show the plots of two experimental stress-strain curves from CuAl single crystals. The stress-strain curve in Fig. 2(a) corresponds to the medium strain rates, while that in Fig. 2(b) is for high applied strain rates. The stress-time series in the intermediate and high strain rate regimes from the model are shown in Figs. 2(c) and 2(d). The similarity between the experimental time series and that of the model is clear.

The analysis of the stress-time series given in Fig. 2(a) has been reported in Ref. [20]. The correlation dimension was found to be $\nu = 2.3$. Then, the number of degrees of freedom required for the description of the dynamics of the system, given by the minimum integer larger than $\nu+1$ [41], is seen to be four, consistent with that used in the original

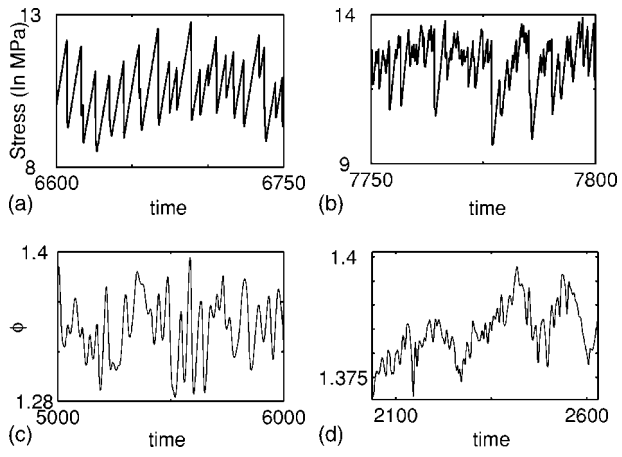

FIG. 2. Experimental stress-time series: (a) chaotic state at strain rates $\dot{\epsilon}_a = 1.7 \times 10^{-5} s^{-1}$ and (b) power-law state at $\dot{\epsilon}_a = 8.3 \times 10^{-5} s^{-1}$. Stress-time series from the model at (c) $\dot{\epsilon} = 120$ and (d) $\dot{\epsilon} = 280$.

model. This time series also has one positive Lyapunov exponent, and hence, is chaotic [20]. As an independent check to obtain the number of degrees of freedom, as also for the visualization of the experimental attractor, we have carried out singular value decomposition of this time series. The normalized eigenvalues are shown in Fig. 3, which shows that the relative strength of the fourth eigenvalue drops more than 2 orders of magnitude compared to the first, and changes very little beyond the fourth. Thus, we estimate the dimension of the experimental attractor to be four, which is again consistent with that obtained from the correlation dimension. (For time series from model systems, one usually finds a floor level below which the eigenvalues saturate. This is taken as the dimension of the actual attractor. However, in real situations, as in the present case, the eigenvalues do not saturate, due to the presence of noise.) Then, for the visualization of the experimental attractor, we can use the dominant eigenvalues to reconstruct the nature of the attractor. Using the first three principal directions of the subspace $C_i; i = 1-3$, we have reconstructed the experimental attractor in the space of specifically chosen directions $C_1 - C_2, C_3$, and C_1 to permit comparison with the attractor obtained from the model. This is shown in Fig. 4(a) for the experimental time

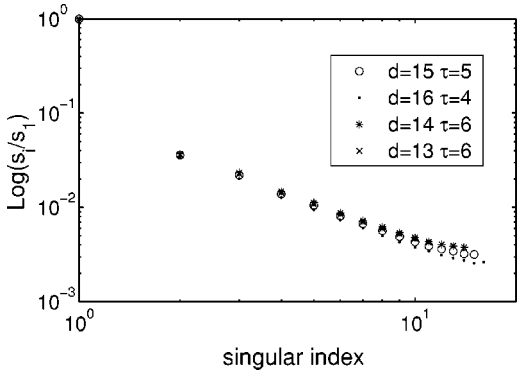

FIG. 3. Singular value spectrum of the experimental time series shown in Fig. 2(a).

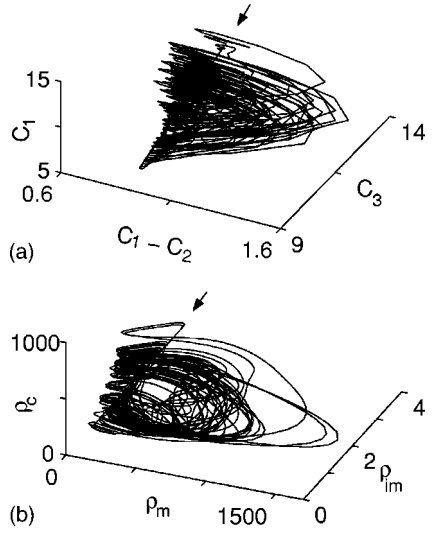

FIG. 4. (a) Reconstructed experimental attractor from the time series shown in Fig. 2(a). (b) Attractor from the model for $N=100$, $j=50$.

series at $\dot{\epsilon}_a = 1.7 \times 10^{-5} s^{-1}$. This can be compared with the strange attractor obtained from the model in the space of ρ_m, ρ_{im}, and ρ_c (at an arbitrary spatial location, here $j=50$ and $N=100$) shown in Fig. 4(b) for $\dot{\epsilon}=120$, corresponding to the midchaotic region (see below). Note the similarity with the experimental attractor, particularly about the linear portion in the phase space [Fig. 4(a)]. This direction can be identified with the loading direction in Fig. 2(a). Note that the identification of the loading direction is consistent with the relatively low values of ρ_m. Thus, it appears that the model is chaotic at low and medium strain rates. As a confirmatory test, we shall study the Lyapunov spectrum of the model in the next section.

In contrast to the experimental time series at low and medium strain rates, for the time series at the highest $\dot{\epsilon}_a$ [Fig. 2(b)], as shown in Ref. [20], we neither find a positive Lyapunov exponent nor a converged value of the correlation dimension. Instead, the distribution of stress drops obeys a power law [20] (see also Fig. 5). We shall refer to this as the power-law regime of stress drops.

We now address if the model generates power-law statistics of stress drops. It is clear that Fig. 2(d) is similar to Fig. 2(b), as there is no inherent scale in the magnitudes of the

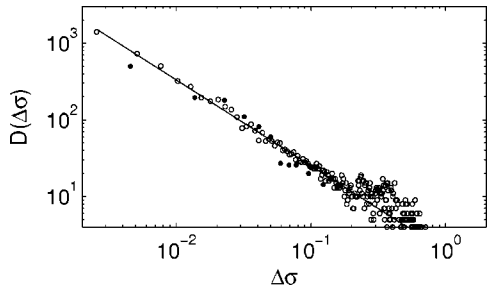

FIG. 5. Distributions of the stress drops from the model (○), from experiments (●) for $N=1000$, and $\dot{\epsilon}=280$. The solid line is a guide to the eye.

stress drops in both cases, and thus, it is likely that stress-strain curves from the model in the high strain rate regime may also exhibit power law statistics of stress drops. Indeed, the distribution of stress drop magnitudes, $D(\Delta\phi)$, shown in Fig. 5 and obtained from long runs for a large system size ($N=1000$), shows a power law $D(\Delta\phi) \sim \Delta\phi^{-\alpha}$ over 2 orders of magnitude, which increases with both the length of stress series and the system size. [Note that the value of N here is nearly three times larger than the results in Ref. [31], Fig. 3(b), and thus, the power law is well converged with respect to the system size.] Surprisingly, experimental points (•) corresponding to $\dot{\epsilon}_a = 8.3 \times 10^{-5} s^{-1}$ also fall on the same curve with an exponent value $\alpha \approx 1.1$. (We have scaled the experimental points by a constant amount along both axes to show that these points also fall on the same line.) The distribution of the durations of the stress drops $D(\Delta t) \sim \Delta t^{-\beta}$ also shows a power law with an exponent value $\beta \approx 1.3$. The conditional average of $\Delta\phi$, denoted by $\langle \Delta\phi \rangle_c$ for a given value of Δt, behaves as $\langle \Delta\phi \rangle_c \sim \Delta t^{1/x}$ with $x \approx 0.65$. The exponent values satisfy the scaling relation $\alpha = x(\beta - 1) + 1$ quite well. The exponent values that remain unaltered in the region of strain rate $270 < \dot{\epsilon} < 700$ we have investigated thus are *independent of the value of the drive parameter*. (There are models of coupled-map lattices that produce power laws, where the exponent value depends on the drive parameter.) We now investigate the underlying causes leading to this power law.

VI. DYNAMICS OF CROSSOVER

A. Lyapunov spectrum

While it is pleasing to see that the model does generate the power-law distribution of stress drops at high strain rates, we still do not know the mechanism responsible for this. An answer to this is particularly important, as the model is fully dynamical and noise free.

In order to answer the question, and also to characterize the dynamics of crossover, we follow the evolution of the Lyapunov spectrum as a function of the applied strain rate in the entire interval where the PLC effect is seen. Further, we also discuss the convergence properties of the Lyapunov spectrum as the system size is increased. In particular, this will be useful in examining the density of null (nearly vanishing) exponents and also to compare our results with that of the shell model of turbulence.

We have calculated the spectrum of Lyapunov exponents using the algorithm by Benettin *et al.* [43]. The exponent values reported here were obtained by averaging over 15 000 time steps after stabilization with an accuracy of 10^{-6}. We have used several system sizes ranging from $N = 100, 150, 350, 500, 1000$, and 3333, which cover approximately two orders of magnitude in M, i.e., from 301 to 10 000. A rough idea of the changes in the dynamics of the system can be obtained by studying the dependence of the largest Lyapunov exponent, λ_{max}, as a function of the strain rate. The largest Lyapunov exponent converges fast as a function of the system size. For instance, we find that λ_{max} for $N=500$ looks the same for a much smaller system size $N=100$ given in Fig. 3(a) in Ref. [31]. (Indeed, one of the

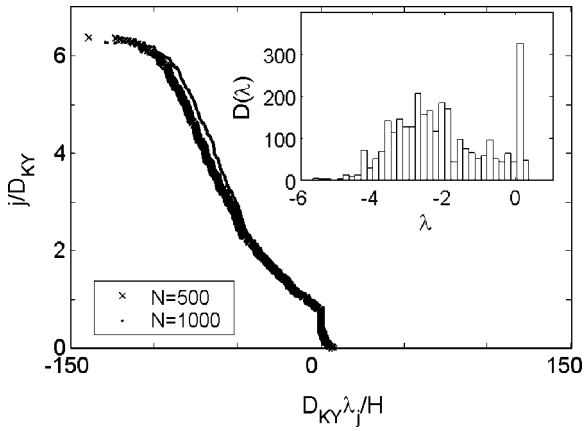

FIG. 6. A plot of j/D_{KY} vs $\lambda_j D_{KY}/H$ for $\dot{\epsilon}=120$. The inset shows a plot of $D(\lambda)$ as a function of λ for $N=1000$.

primary requirements for spatially extended systems is the convergence of the largest Lyapunov exponent as a function of system size [27].) $\lambda_{\max}$ becomes positive around $\dot{\epsilon}\approx 35$, reaching a maximum at $\dot{\epsilon}=120$, and practically vanishing around 250. (Periodic states are observed in the interval $10<\dot{\epsilon}<35$.) In the region $\dot{\epsilon}\geqslant 250$, the dispersion in the value of $\lambda_{\max}$ is $\sim 5\times 10^{-4}$, which is the same order as the mean. Thus, $\lambda_{\max}$ can be taken to vanish beyond $\dot{\epsilon}=250$.

The study of the Lyapunov spectrum reveals that in the chaotic regime of strain rates, only a small proportion of the exponents are positive, an equal small number are close to zero, and a large proportion of the exponents are negative. The distribution of the Lyapunov exponents $D(\lambda)$ is shown for $N=1000$ in the inset of Fig. 6 for $\dot{\epsilon}=120$. For this system size (with a total of exponents $M=3001$), the number of positive exponents is $\approx$ 6.2% of the total number of exponents, and the null exponents are also $\approx$9%. (For numerical purposes null exponents are taken to correspond to $|\lambda| \leqslant 5.2\times 10^{-4}$.) These ratios remain the same for the larger system sizes used.

While $D(\lambda)$ reflects the distribution of Lyapunov exponents in various regions, for studying the convergence of the Lyapunov spectrum, plots of the density function $j/D_{KY} = f(\lambda_j D_{KY}/H)$ are better suited. Further, these quantities have been used traditionally in the studies of extended dynamical systems [27]. A plot of j/D_{KY} vs $\lambda_j D_{KY}/H$ for $\dot{\epsilon}=120$ for $N=500$ and 1000 is shown in Fig. 6. It is clear that while the density function has not yet converged for negative values of $\lambda_j D_{KY}/H$, those for positive values are already converged. As we increase the strain rate beyond $\dot{\epsilon}=180$, concomitant with the decrease in the value of $\lambda_{\max}$, the number of null exponents increases. For instance, at $\dot{\epsilon}=220$, for which the maximum Lyapunov exponent is small, $\sim$0.0058, the number of null exponents increases to 30% M (see inset of Fig. 7). $D(\lambda)$ shows that the number of null exponents has increased. Concomitant with this trend, a plot of j/D_{KY} vs $\lambda_j D_{KY}/H$ for $N=500$ and 1000 (Fig. 7) shows that for $\dot{\epsilon}=220$ is well converged for the entire range of values of the scaled Lyapunov exponent $\lambda_j D_{KY}/H$. This signals a faster convergence of the density function $j/D_{KY}=f(\lambda_j D_{KY}/H)$ with the system size, as we approach the scaling regime. Indeed, we find that plots for $N=500$ and 1000 for strain rate $\dot{\epsilon}=280$ cannot be distinguished over the entire range of values of $\lambda_j D_{KY}/H$. Even though it would be adequate to use $N=1000$ for a further analysis of the Lyapunov spectrum in the scaling regime, we use a much bigger system size of $N=3333$, which for all practical purposes can be taken to be large N limit. A plot of j/D_{KY} vs $\lambda_j D_{KY}/H$, shown in Fig. 8 for $N=3333$ (and also for 1000), shows that for $\dot{\epsilon}=280$ is well converged for the entire range of values of $\lambda_j D_{KY}/H$. Note also that nearly 40% of the exponents are close to zero (see the inset).

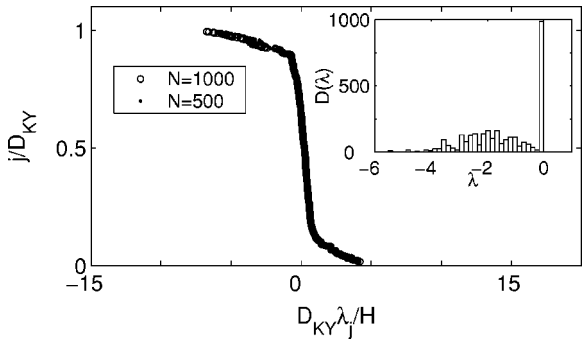

FIG. 7. A plot of j/D_{KY} vs $\lambda_j D_{KY}/H$ for $\dot{\epsilon}=220$. The inset shows a plot of $D(\lambda)$ as a function of λ for $N=1000$.

As we approach the power-law regime of stress drops (extending from $\dot{\epsilon}=250$), as the largest Lyapunov exponent approaches zero ($\sim 5.16\times 10^{-4}$ for $\dot{\epsilon}=280$), exponents below a certain value cross each other as a function of time; the distribution of the exponents remains unchanged. However, the first few exponents remain distinct. Figure 9 shows the first two exponents that are well separated and another two which are close to each other in magnitude (for $\dot{\epsilon}=280$ and $N=3333$). The most significant feature of the spectrum in the region is that there is a *dense set of null exponents*. The peaked nature of the distribution of the null exponents ($|\lambda| \leqslant 5.2\times 10^{-4}$) for $\dot{\epsilon}=280$ is shown in Fig. 10.

The peaked nature of $D(|\lambda|)$ for the null exponents suggests a power-law distribution for their magnitudes. The distribution of the null exponents ($|\lambda_i|\leqslant 5.2\times 10^{-4}$) for $\dot{\epsilon}=280$, for a system size of $N=3333, M=10\,000$ is shown in Fig. 11. It is clear that both positive and negative exponents show a power-law distribution $D(|\lambda|)\sim|\lambda|^{-\gamma}$ with an exponent value $\gamma\sim 0.51$, and the scaling extends over an impressive three decades. As null exponents correspond to marginal stable

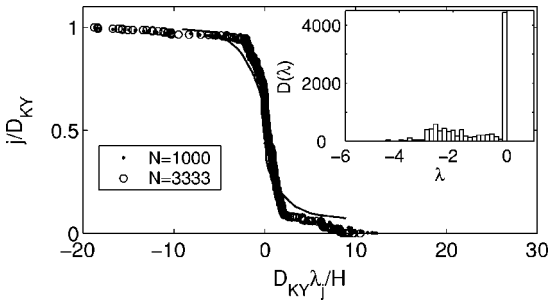

FIG. 8. A plot of j/D_{KY} vs $\lambda_j D_{KY}/H$ for $\dot{\epsilon}=280$. The inset shows a plot of $D(\lambda)$ for $N=3333$. A schematic plot of the Lyapunov density function (continuous line) for the shell model (after [28]) is shown.

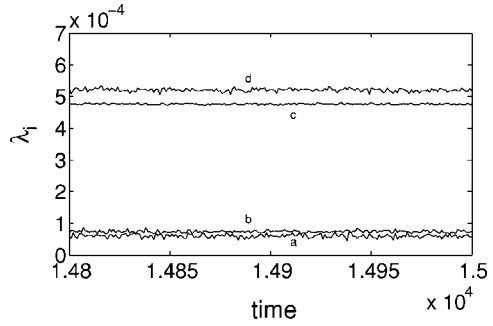

FIG. 9. The first two Lyapunov exponents that do not cross each other as a function of time for $N=3333$ for $\dot{\epsilon}=280$. Also shown are two more exponents that are close to each other.

natures of the system, their finite density, which itself obeys a power-law, elucidates the underlying cause of power-law distribution of stress drops at high strain rates.

B. Comparison with shell model for turbulence

As mentioned in the Introduction, both in the PLC effect and in turbulence, power-law statistics are seen at high drive rates in contrast to conventional SOC systems, where it is observed at low drives [24]. Such finite-density null Lyapunov exponents were suggested by Ruelle [44] in the context of turbulence. This property is preserved by the shell model [28]. Here we attempt a comparison of the Lyapunov spectrum obtained from our model with that of the shell model.

Shell models of turbulence [27] are designed to mimic the behavior of Navier-Stokes equations at high drives, where the power law is seen. One standard shell model is the Gledzer-Ohkitani-Yamada model [27,28]. For this model, Ohkitani and Yamada [28] gave good numerical evidence that the density function exists as the viscosity parameter η tends to zero. In our case, the role of the viscosity parameter is taken by the applied strain rate. In Sec. IV A we have shown that there is a rapid increase in the density of null exponents and consequently, there is a rapid convergence of $j/D_{KY}=f(\lambda_j D_{KY}/H)$ as a function of N, starting from $\dot{\epsilon}=220$. This suggests that one should expect convergence of the limiting $j/D_{KY}=f(\lambda_j D_{KY}/H)$ function as we approach the power-law strain rate regime of stress drops. Thus, we should

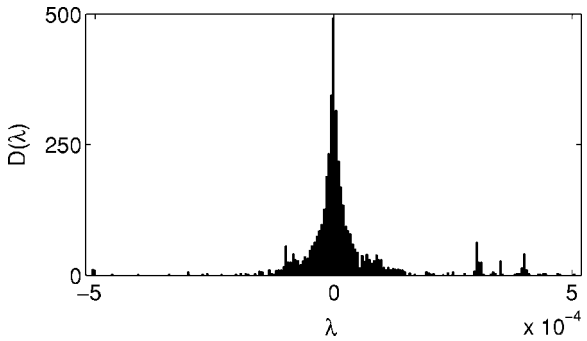

FIG. 10. The peaked nature of the distribution of null exponents lying in the range $[-5.2\times10^{-4},5.2\times10^{-4}]$ for $\dot{\epsilon}=280, N=3333$.

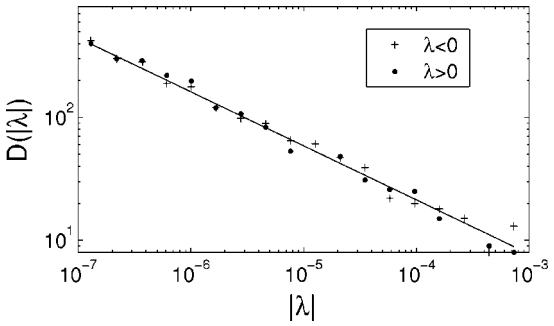

FIG. 11. Log-log plot of the distribution of the marginal exponents for $\dot{\epsilon}=280, N=3333$. The solid line is a guide to the eye.

expect that the limiting distribution itself converges as a function of $\dot{\epsilon}$ as we approach the scaling regime. Considering $N=1000$ approximates the limiting distribution (see Fig. 7 for justification), we have verified that plots of $j/D_{KY}=f(\lambda_j D_{KY}/H)$ for three values of $\dot{\epsilon}=250$, 260, and 280 for reasonably large $N=1000$ converge. This result is similar to the convergence of the density function in the shell model as a function of the viscosity parameter. The density function j/D_{KY} obtained from the model can be compared with that of the shell model. A plot of $j/D_{KY}=f(\lambda_j D_{KY}/H)$ for a large system $N=3333$ (which can be taken to represent the limiting density as a function of system size) for $\dot{\epsilon}=280$ is shown in Fig. 8, along with a schematic plot for the shell model shown by the continuous line. As can be seen, in both cases, the distribution function that is proportional to $-df(\lambda)/d\lambda$ shows a singularity near zero, the difference being that the singularity is more pronounced for our model. Ohkitani and Yamada also plot another quantity that represents the null exponents better, namely, the sum of Lyapunov exponents up to j, normalized by H as a function of j scaled by D_{KY}. The quantity $\Sigma_1^j \lambda_j/H$ is an increasing function of j/D_{KY} for positive λ_j and goes to unity when $\Sigma_{i=1}^j \lambda_i = H$. In the region of null exponents, this quantity remains constant and then decreases with j for negative λ_j. Thus, $\Sigma_1^j \lambda_j/H$ also reflects the density of null exponents. A schematic plot of $\Sigma_1^j \lambda_j/H$ as a function of j/D_{KY} (continuous and dashed line) for the shell model is shown in Fig. 12. The increase in $\Sigma_1^j \lambda_j/H$ for small j/D_{KY} shows that there is a finite density of positive expo-

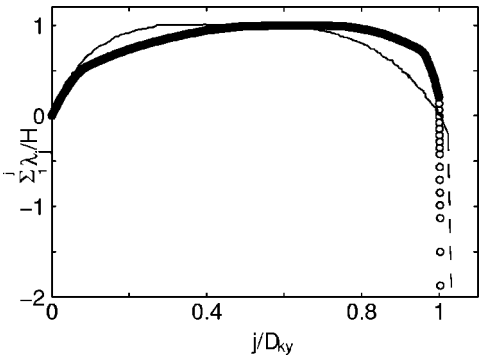

FIG. 12. A plot of $\Sigma_1^j \lambda_j/H$ as a function of j/D_{KY} for $\dot{\epsilon}=280$ and $N=3333$. The corresponding schematic plot for the shell model for $j/D_{KY}<1$ (continuous line) and $j/D_{KY}\geqslant 1$ (dashed curve) (after [28]) is shown.

nents in the Lyapunov spectrum for the shell model. Further, these authors find that there is a convergence with respect to the viscosity parameter for the Lyapunov spectrum corresponding to the interior of the attractor (i.e., $j/D_{KY}<1$), while there is scatter for $j/D_{KY}>1$ (the dashed line represents this portion). We have plotted $\Sigma_1^j \lambda_j/H$ as a function of j/D_{KY} for $N=3333$ on the same plot for the sake of comparison. In our case, the increase to unit value is much slower (compared to the shell model), which clearly implies that there are very few positive exponents (of any significant magnitude) with most of them being vanishingly small. This feature is unlike the shell model, where there is a finite density of positive exponents. In the shell model, the largest exponent is proportional to $\eta^{-1/2}$, which is reflected in the steeper increase in $\Sigma_1^j \lambda_j/H$ for the shell model.

C. Slow manifold analysis

The above analysis shows that as the strain rate is increased, most exponents get concentrated around the zero value. As zero Lyapunov exponents represent a marginal situation, the region of $\dot{\epsilon}>240$ (corresponding to the power-law state of stress drops) can be identified with a marginally stable state. Thus, it would be interesting to realize a geometrical picture of dislocation configurations in the marginal state and examine how dislocations reach this state with increasing strain rate.

Recently, the geometry of the slow manifold [38] of the original model has been examined in detail [14,34]. The study shows that the relaxational nature of the PLC effect arises from the *atypical bent nature of the slow manifold*. Here, we recall some relevant results on the slow manifold of the original model ($D=0$) and extend the ideas to the spatial extension of model ($D\neq 0$). Slow manifold expresses the fast variable in terms of the slow variables, conventionally done by setting the derivative of the fast variable to zero [14,34],

$$\dot{\rho}_m = g(\rho_m, \phi) = -b_0\rho_m^2 + \rho_m\delta + \rho_{im} = 0, \tag{9}$$

where $\delta=\phi^m-\rho_{im}-a$. δ has been shown to have all the features of an effective stress and thus plays an important physical role [34], particularly in studying the pinning-unpinning of dislocations. We note that δ is a combination of two slow variables ϕ and ρ_{im}, both of which take small positive values. Hence, δ takes on small positive and negative values. Using Eq. (9), we get two solutions:

$$\rho_m = [\delta + (\delta^2 + 4b_0\rho_{im})^{1/2}]/2b_0, \tag{10}$$

one for $\delta<0$ and another for $\delta>0$. For regions of $\delta<0$, as b_0 is small $\sim 10^{-4}$, we get $\rho_m/\rho_{im}\approx -1/\delta$, which takes on small values. This defines a part of the slow manifold, S_2, where ρ_m is small. In this region, as the mobile density is small and immobile density is large (relative to ρ_m), this region can be identified with pinned configuration of dislocations and hence we shall refer to the region S_2 as the "*pinned state of dislocations*." We note that larger negative values of δ correspond to strongly pinned configurations, as they refer to smaller ratio of ρ_m/ρ_{im}. For positive values of δ, another connected piece, S_1, is defined by *large values* of ρ_m, given by $\rho_m\approx\delta/b_0$, which we refer to as the "*unpinned state of dislocations*," as ρ_{im} is also small. These two pieces, S_2 and S_1, are separated by $\delta=0$, which we refer to as *the fold line* [14,34] (see below). A plot of the slow manifold in the $\delta-\rho_m$ plane is shown in Fig. 13(a). For the sake of illustration, we have plotted a monoperiodic trajectory describing the changes in the densities during a loading-unloading cycle. The inset shows $\rho_m(t)$ and $\phi(t)$. For completeness, the corresponding plot of the slow manifold in the $(\rho_m, \rho_{im}, \phi)$ space is shown in Fig. 13(b), along with the trajectory and the symbols. In this space, one can see that $\delta=\phi^m-\rho_{im}-a=0$ is a line that separates the pieces S_2 and S_1 of the slow manifold, and hence the name *fold line*. The cyclic changes in the variables is well captured by the nature of trajectory shown in Fig. 13(b). The trajectory enters S_2 at A and moves into S_2. The value of δ [in Fig. 13(a)] decreases from zero to a maximum negative value as the trajectory reaches B. Then, δ increases as the trajectory returns to A' before leaving S_2. The corresponding segment is ABA' in Fig. 13(b), which is identified with the flat region of $\rho_m(t)$ in the inset of Fig. 13(a). As the trajectory crosses $\delta=0$, $\partial g/\partial\rho_m$ becomes positive and accelerates into the shaded region [Fig. 13(a)] rapidly until, it reaches $\rho_m=\delta/2b_0$. Thereafter, it settles down quickly on S_1, decreasing rapidly until it re-enters S_2 again at A. The burst in ρ_m [inset in Fig. 13(a)] corresponds to the segment $A'DA$ in Figs. 13(a) and 13(b). The nature of trajectories in the chaotic domain is essentially the same, but is different in the power-law regime of high strain rates, as we will show later.

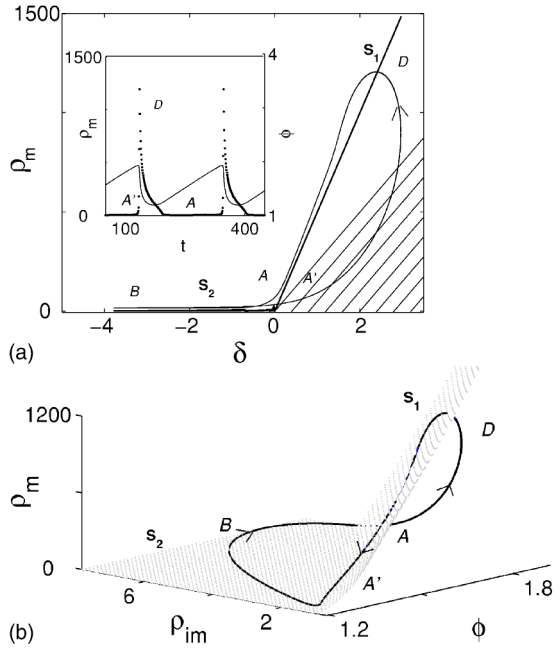

FIG. 13. (a) Bent slow manifold S_1 and S_2 (thick lines) with a simple trajectory for $\dot{\epsilon}=200$ and $m=3$. Inset: ρ_m (dotted curve) and ϕ (solid line). (b) The same trajectory in the $(\phi, \rho_{im}, \rho_m)$ space.

We now consider the variation of stress as the state of the system changes from the pinned to the unpinned state, i.e., when the system goes though a burst of plastic activity. For $D=0$, Eq. (6) reduces to

$$\dot{\phi} = d[\dot{\epsilon} - \dot{\epsilon}_p], \tag{11}$$

where $\dot{\epsilon}_p = \phi^m \rho_m$ is the plastic strain rate. Since ρ_m is small and nearly constant on the pinned state S_2, stress increases monotonically. However, during the burst in ρ_m ($A'DA$ in the inset), $\dot{\epsilon}_p(t)$ exceeds $\dot{\epsilon}$, leading to a yield drop. Since ρ_m grows outside S_2, the $\delta=0$ line separates the pinned state from the unpinned state. Thus, $\delta=0$ *physically corresponds to the value of the effective stress at which dislocations are unpinned*.

When the spatial degrees of freedom are included, there is no additional complication as the slow manifold is defined at each spatial point. Thus, a convenient set of variables for the visualization of dislocations is, $\rho_m(x), \delta(x), x$. Here, we investigate the nature of typical spatial configurations in the chaotic and the power-law regimes of stress drops and study the changes as we increase the strain rate. For simplicity, we shall use $h=0$ for which we have $\phi_{eff}=\phi$. (It is straightforward to extend the arguments to the case when $h \neq 0$.) Then, the plastic strain rate $\dot{\epsilon}_p(t)$ is given by

$$\dot{\epsilon}_p(t) = \phi^m(t)\frac{1}{l}\int_0^l \rho_m(x,t)dx = \phi^m(t)\overline{\rho_m}(t), \tag{12}$$

where $\overline{\rho_m}(t)$ is the mean mobile density [$=\Sigma_j \rho_m(j,t)/N$ in the discretized form]. With the inclusion of spatial degrees of freedom, the yield drop is controlled by the spatial average $\overline{\rho_m}(t)$, rather than by individual values of $\rho_m(j)$. Further, although the configuration of dislocations change during one loading-unloading cycle, the drastic changes occur during a yield drop when $\overline{\rho_m}(t)$ grows rapidly. However, one should expect that configurations will be representative for a given strain rate. Thus, we focus our attention on the spatial configurations on the slow manifold *at the onset and at the end of a typical yield drop*.

First, consider the configuration seen just before and after the yield drop when the strain rate is in the chaotic regime. In this regime, the stress drop magnitudes are large, implying that the change in mobile density is large. Figures 14(a) and 14(b) for a typical value of $\dot{\epsilon}=120$. It is clear that both at the onset and end of a typical large yield drop, the $\delta(j)$ values that reflect the state of system (pinned or unpinned state), are negative, and correspondingly, the mobile density $\rho_m(j)$'s are small, i.e., most dislocations are in *a strongly pinned state*. (Recall that δ signifies how close the spatial elements are close to unpinning threshold.) The arrows show the increase in $\rho_m(j)$ at the end of the yield drop. We have checked that this is a general feature for all yield drops in the chaotic regime of strain rates. Now consider a dislocation configuration in the scaling regime at high strain rates, say, $\dot{\epsilon}=280$, at the onset and end of a yield drop shown in Figs. 14(c) and 14(d) respectively. In contrast to the chaotic regime, in the scaling regime, *most dislocations are clearly seen to be at the threshold of unpinning with* $\delta(j) \approx 0$, both at the onset and end of the yield drop. This also implies that they remain close to this threshold throughout the process of a stress drop. We have verified that the *edge-of-unpinning picture is valid* in the entire power-law regime of stress drops for a range of N values. Further, as a function of strain rate, we find that the number of spatial elements reaching the threshold of unpinning $\delta=0$ during a yield drop increases as we approach the scaling regime of stress drops.

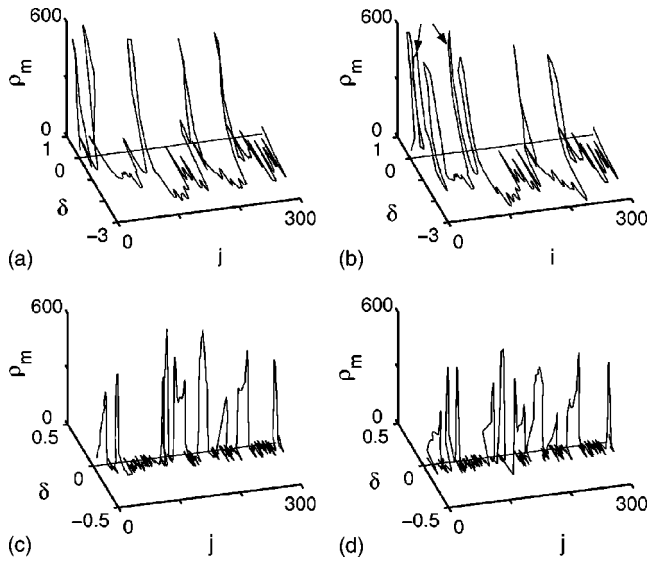

FIG. 14. Dislocation configurations on the slow manifold at the inset and at the end of yield drop: (a) and (b) for $\dot{\epsilon}=120$ (chaotic regime), and (c) and (d) for $\dot{\epsilon}=280$ (scaling regime).

VII. TYPES OF BANDS

As the extended Ananthakrishna's model is able to reproduce the crossover dynamics from chaos to the power-law regime of stress drops (and other generic features demonstrated earlier), one might expect that the nature of the different types of bands may also emerge. Most models of dislocation bands use diffusive coupling, although the physical mechanism of the term is different in different situations [1]. An important feature of the spatial coupling in the model is that it accounts for the spreading of dislocations into regions of low back stress once dislocations are unpinned (the factor ρ_{im}^{-1}). The term also determines the length scale over which dislocations spread into the neighboring elements. Thus, while dislocation pinning and unpinning gives a heterogeneity in space (in principle), regions of low ρ_{im} are favored for dislocation multiplication and spreading into such regions. Further, this type of spatial term couples length and time scales in a dynamical way, as ρ_{im} itself evolves in time and hence, the associated time scale. Indeed, multiplication of dislocation depends on stress, (i.e., ϕ_{eff}^m), and hence this rate itself is changing dynamically, leading to changes in the time scale of internal relaxation as a function of $\dot{\epsilon}$. This leads to changes in spatial correlation as the strain rate is increased.

Below, we report both numerical and analytical studies on the spatiotemporal patterns emerging from the model as a function of the strain rate, $\dot{\epsilon}$. We begin with the numerical results [45].

For $\dot{\epsilon}<10$ and $\dot{\epsilon}>2000$, we get homogeneous steady-state solutions for all the dislocation densities, ρ_m, ρ_{im}, and ρ_c. In the region where interesting dynamics of chaotic and power-law states are observed, the nature of the dislocation

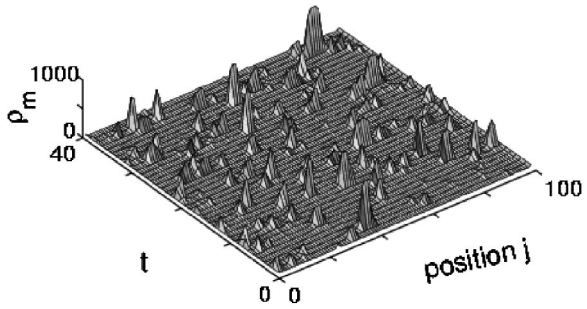

FIG. 15. Spatially uncorrelated bands at $\dot{\epsilon}=40$.

bands can be broadly classified into three different types occurring at low, intermediate, and high strain rates described below.

For strain rates $30 \leqslant \dot{\epsilon} < 70$, we get uncorrelated static dislocation bands. The features of these bands are illustrated for a typical value, say for $\dot{\epsilon}=40$ in Fig. 15. Dislocation bands of finite width nucleate randomly in space and remain static until another band is nucleated at another spatially uncorrelated site. The associated stress-time curve that is nearly regular has large characteristic stress drops whose distribution is peaked as in experiments at low strain rates [21].

At slightly higher values of strain rates, $70 \leqslant \dot{\epsilon} < 180$, we find that new bands nucleate ahead of the earlier ones, giving a visual impression of *hopping bands*. This can be clearly seen from Fig. 16, where a plot of $\rho_m(j,t)$ is given for $\dot{\epsilon}=130$. However, this hopping motion does not continue until the other boundary. They stop midway and another set of hopping bands reappear in the neighborhood. Often nucleation occurs at more than one location. Stress-time plots in this regime have a form similar to Fig. 2(c), with the average amplitude of the stress drops being smaller than the localized nonhopping bands at low strain rates as seen in experiments. The distribution of stress drops is nearly symmetric but slightly skewed to the right, similar to those observed in experiments [21].

As the strain rate is increased further, the extent of propagation increases, concomitantly, and the magnitudes of the stress drops decrease. We see continuously propagating bands even at $\dot{\epsilon}=240$, as can be seen from Fig. 17. One can see dislocation bands nucleating from one end of the sample ($j=0$, $t=20$, 40, and 60) and propagating continuously to the other end. Often, we see a band nucleating at a point,

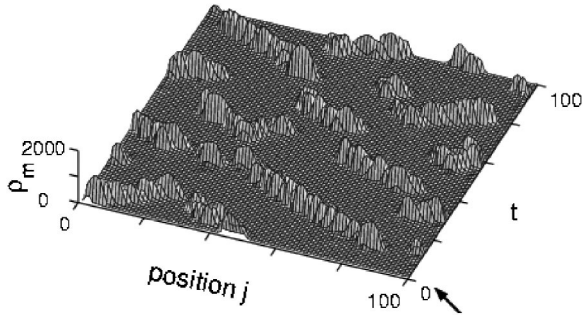

FIG. 16. Hopping-type bands at $\dot{\epsilon}=130$ (arrow shows one such band).

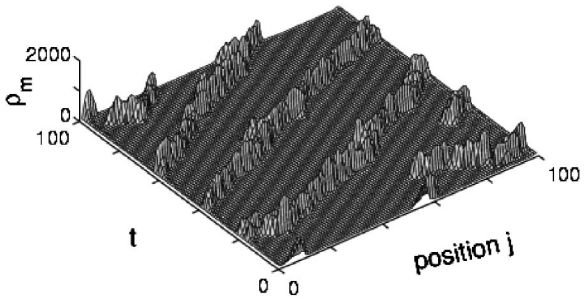

FIG. 17. Fully propagating bands at $\dot{\epsilon}=240$.

branching out, and propagating only partially towards both the ends. Unlike the present case, which exhibits rather uniform values of ρ_m, we usually find irregularities as the band reaches the edges. The stress strain curve in this region of strain rates exhibits a scale-free feature in the amplitude of the stress drops similar to Fig. 2(d), with a large number of small drops. As can be seen from Fig. 2(d), the mean stress level of these small amplitude stress drops increases until a large yield drop is seen. This large stress drop corresponds to bands having reached the end of the specimen.

It is possible to calculate the velocity of the propagating bands in the high strain rate limit. We first note that our equations constitute a coupled set of integropartial differential equations, and hence cannot be dealt with in their present form. To reduce these equations to a form that is suitable for further analysis, we recall a few pertinent points about the changes in the structure of the slow manifold as a function of the applied strain rate. We note that the original model exhibits an incomplete approach to homoclinicity [34], i.e., the number of mixed mode oscillations of the type L^s are limited, where L and s refer to the large and small amplitude oscillations, respectively. Typically, about 12 small amplitude, nearly harmonic, oscillations are known to occur for a single large one at high values of the strain rate. The reason attributed to the limited number of small loops is the finite rate of softening of the eigenvalue of the fixed point as the reverse Hopf bifurcation is reached [34]. In the presence of the spatial coupling we find that the softening rate is further enhanced, as is clear from the fact that the upper Hopf bifurcation is pushed to much larger values of strain rate ($\dot{\epsilon}_{c_2}=2000$, see Fig. 1). This enhanced softening rate implies that the number of small amplitude oscillations is also increased in this domain of strain rates. Even so, the geometry of the slow manifold is not altered from that of the space-independent model. In particular, the position of the unstable saddle focus remains located on the S_1 part of the manifold (Refs. [14,34]). In addition, the feature of the fixed point approaching the fold line as a function of the strain rate is retained. Under these conditions, for high strain rates, nearly sinusoidal oscillations are executed around the fixed point with the orbits touching S_2 only after executing several such turns. A plot of this is shown in Fig. 18. We further recall that our analysis shows that the orbit is reinjected along the stable manifold close to the unstable saddle focus (as shown in Fig. 11 of Ref. [34]). The orbit then spirals out along the unstable manifold of the fixed point. Once the orbit is sufficiently away from the fixed point when the influence of the fixed

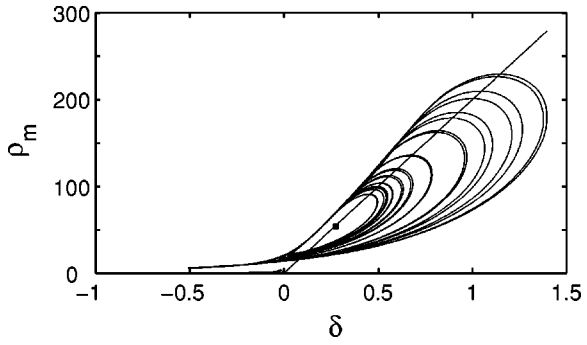

FIG. 18. Slow manifold showing a trajectory for the space-independent model near the reverse Hopf bifurcation point, at $\dot{\epsilon}=90$, $m=2$. • fixed point of Eqs. (1)–(3) and (6).

point is lost, it is reinjected close to the fixed point via S_1. The dynamics then repeats. Note that at high applied strain rates, the system is close to the reverse Hopf bifurcation point and hence the fixed point is close to the applied strain rate value. Thus, as the orbit executes one turn, there is one small yield drop. However, the orbit executes several turns around the fixed point, each turn leading to larger loop sizes, i.e., larger values of ρ_m. Consequently, it leads to successively larger stress levels than the earlier one before briefly visiting S_2.

Under these conditions the dynamics is entirely controlled by the spiraling motion around the fixed point. Thus, the entire dynamics is essentially described by the fast variable; the other two variables ρ_{im} and ϕ can be taken to be parameters. Such a situation is described by the transient dynamics dictated entirely by equation of the fast variable (the so-called layer problem [38]) and thus, we are justified in using only the evolution equation of the fast variable in terms of the slow manifold parameter $\delta=\phi^m-\rho_{im}-a$. Since the trajectory rarely visits the S_2 part of the slow manifold, we restrict the calculations to $\delta>0$. The physical picture of a propagating solution is that, as the orbit at a site makes one turn around the fixed point, i.e., δ small but positive, around the value of the applied strain rate, the front advances by a certain distance along the specimen like the motion of a screw.

The rate equation for ρ_m in terms of δ is

$$\frac{\partial \rho_m}{\partial t} = -b_o\rho_m^2 + \delta\rho_m + \rho_{im} + D'\frac{\partial^2\rho_m}{\partial x^2}, \tag{13}$$

where $D'=D\phi^m/\rho_{im}$. Since, the slow variables ρ_{im} and ϕ are treated as parameters, this has the form of a Fisher-Kolmogorov equation for propagating fronts. This equation can be reduced to the standard form,

$$\frac{\partial Z}{\partial t'} = Z(1-Z) + D'\frac{\partial^2 Z}{\partial x^2}. \tag{14}$$

(This is done by first transforming $\rho_m=X-\rho_{im}/\delta$, dropping the term $2b_0\rho_{im}/\delta$ compared to δ in the linear term in X, and then using $Z=X\delta/b_0$ and $t'=t\delta$.) It is clear that $Z=0$ is unstable and $Z=1$ is stable. Using the form for propagating front $Z=Z_oe^{\omega t'-kx'}$, the marginal velocity is calculated using $v^*=\mathrm{Re}\ \omega(k^*)/\mathrm{Re}\ k^*=d\omega/dk|_{k=k^*}$ and $\Im d\omega/dk|_{k=k^*}=0$, gives the velocity of the bands $v^*=2$ [46,47]. In terms of the variables in Eq. (13), the marginal velocity is

$$v^* = 2\sqrt{D\delta}. \tag{15}$$

In order to relate this to the applied strain rate, we note that for a fixed value of the strain rate (where propagating bands are seen), the average level of stress drop is essentially constant. Thus, from Eq. (6), we see that in this regime of high strain rates, the applied strain rate $\dot{\epsilon}$ is essentially balanced by the plastic strain rate $(1/l)\int_0^l\phi^m\rho_m(x,t)\equiv\dot{\epsilon}_p$. Then, using $\phi^m=\dot{\epsilon}/\overline{\rho_m}$, and using $\delta=\phi^m-a-\rho_{im}$, we get

$$v = 2\sqrt{\frac{D\dot{\epsilon}}{\overline{\rho_m}\rho_{im}}\left(\frac{\dot{\epsilon}}{\overline{\rho_m}}-a-\rho_{im}\right)}. \tag{16}$$

It is important to note that at high applied strain rate, $\overline{\rho_m}\sim\overline{\rho_m^*}$, the fixed point value. Thus, for all practical purposes, we can assume $\overline{\rho_m}$ as a constant. From the above equation, we see that the velocity of the propagating bands is proportional to the applied strain rate. This result is similar to the result obtained recently by Hähner *et al.* [48]. Further, $v\propto 1/\overline{\rho_m}$, which also appears to be consistent with an old experimental result. (See Fig. 7 of Ref. [49], which appears to fit $v\overline{\rho_m}$=const.) This result needs further experimental support.

As the form of Eq. (14) has the standard form, all other results carry through, including nonlinear analysis. We have numerically calculated the velocity of the continuously propagating bands at high strain rates from the model equations, which confirms the linear dependence of the band velocity on applied strain rate. In the region of strain rates $\dot{\epsilon}=220-280$ (corresponding to unscaled strain rate values $10^{-4}-1.5\times10^{-4}\ s^{-1}$), we find that the unscaled values of the band velocity increases from 100 to 130 μm/s. These values are consistent with the experimental values reported by Hähner *et al.* [48].

We note here that the types of the bands seen in our model are correlated with the two distinct dynamical regimes investigated. The hopping-type bands belong to the chaotic regime, a result consistent with the recent studies on Cu-Al polycrystals [21]. On the other hand, the propagating bands are seen in the power-law regime of stress drops [31], again consistent with these studies [20,21]. Curiously, the uncorrelated bands predicted by the model also belong to the chaotic regime. We shall now explain these results based on the dynamics of the model. We first note that each spatial element is described in the three dislocation densities [Eqs. (1)–(3)]. Consider one of these elements being close to the unpinning threshold, i.e., $\delta=0$. It has been shown earlier that ρ_{im} is out of phase with ρ_m [14,34]. This feature is retained with the spatial coupling as well. When the orbit is about to leave S_2, i.e., when $\rho_m(j)$ is at the verge of a sharp increase, ρ_{im} is largest. However, the extent of the spatial coupling is determined by ρ_{im}^{-1}. But the magnitude of ρ_{im} itself decreases with the applied strain rate, being large at low strain rates [14,34]. Thus, the spatial width of this is small at low $\dot{\epsilon}$ and large at high $\dot{\epsilon}$. Next we note that the growth and decay of $\rho_m(j)$ with j occurs over a short time scale, which is typically of the order of the correlation time, τ_c, of $\phi(t)$. Beyond this time,

the memory of its initial state is lost. Consider an initial state when a band is formed at some location. Before the memory of this initial state decays, if a new band is not created, we get an uncorrelated band. On the other hand, if a new band is created before the memory of the initial state decays, there are two possibilities. If another band is created just before the correlation decays substantially by that time, we get a hopping-type band. If however, even before the burst of $\rho_m(j)$ decreases beyond its peak value, new sources of creation of ρ_m occur, then we end up seeing a propagating band. An analysis of the correlation time shows that it increases with the applied strain rate. Concomitantly, ρ_{im} decreases with $\dot{\epsilon}$, which implies that the spatial correlation increases. (Indeed, the value of ρ_{im} is quite small for large $\dot{\epsilon}$ as we reach the power-law regime of stress drops.) Under these conditions, only partial plastic relaxation is possible in this regime. This discussion clarifies the dynamic interplay of time and length scales. Moreover, as the spatial coupling term allows the spreading of dislocations only into regions of low ρ_{im} or low back stress, the propensity for continuous propagation of the band is enhanced when ρ_{im} is small. In addition, we find higher values of ρ_{im} at the wake of the band, which favor propagation into regions of smaller immobile density, thus also determining the direction of propagation.

VIII. SUMMARY AND CONCLUSIONS

To summarize, detailed numerical and analytical studies on the extended Ananthakrishna's model show that it reproduces all the important features of the PLC effect, including the crossover from a chaotic to a power-law regime observed in experiments. A systematic study of the system size effects of the Lyapunov spectrum demonstrates that the limiting Lyapunov distribution evolves from a set of positive and negative exponents with a few null exponents in the chaotic regime, to a dense set of null exponents as we approach the scaling regime of stress drops. The analysis provides insight into the dynamical causes leading to this crossover. This study is complemented through the slow manifold analysis, which is particularly useful in giving a geometrical picture of the spatial configurations. The study shows that *while dislocations are largely in the pinned state in low and medium strain rates (chaotic domain), most are pushed to the threshold of unpinning as we approach power-law regime of stress drops*. The study also establishes that the model has considerable similarities with the shell model of turbulence [28]. The model also reproduces the major features of the three bands, namely, the randomly nucleated band, the hopping, and propagating types found as the strain rate is increased. It also predicts a linear dependence of the velocity of the band and inverse dependence on the mobile density at high strain rates.

Several observations may be in order on the dynamics of the crossover. We first note that the crossover itself is smooth as the changes in the Lyapunov spectrum are gradual, though occurring in a narrow interval of strain rates (220–250). Second, the power law here is of a purely dynamical origin (see below). This is a direct result of the existence of a reverse Hopf bifurcation at high strain rates. In this regime, due to softening of the eigenvalues (as a function of $\dot{\epsilon}$), the orbits are mostly restricted to the region around the saddle focus fixed point located on the S_1 part of the manifold. This offers a dynamical reason for the smallness of the yield drops in this region [14,34]. Note also that there is a dynamic feedback between the stress determined by Eq. (6) and the production of dislocations in Eq. (1), which provides an explanation for the slowing down of the plastic relaxation. This sets up a competition between the time scale of internal relaxation and the time scale determined by the applied strain rate (essentially Deborah number). We note that while the time scale for internal relaxation is increasing, that due to the applied strain rate is decreasing. Third, our analysis shows that the power-law regime of stress drops occurring at high strain rates belongs to a different universality class compared to SOC systems, as it is characterized by a dense set of null exponents. This must be contrasted with the lack of any characteristic feature of the Lyapunov spectrum in the few models of SOC studied so far [50–52]. Note that most SOC models have noisy drive and hence are not suitable for calculation of Lyapunov spectrum. Of the few where the spectrum can be calculated, no zero and positive exponents, single positive exponent, zero exponent in the large N limit, etc., have been reported [50–52]. (Often, the nature of the largest Lyapunov exponent is inferred based on the similarity of other dynamical invariants [50].)

On the other hand, the PLC effect is similar to hydrodynamic turbulence. For instance, it is interesting to note that in experiments in both cases, the energy input is at a macroscopic scale cascading down to small length scales. Further, the sequence of dynamical states seen as a function increasing drive in our PLC model is similar to that seen in turbulence experiments on helium [26]. In both cases, one sees periodic states $\rightarrow$ chaos $\rightarrow$ power-law state. In more concrete terms, the dense set of null exponents in our model is actually similar to that obtained in shell models of turbulence where the power law is seen at high drive values [28]. However, there are significant differences. First, we note that the shell model [28] cannot explain the crossover, as it is only designed to explain the power-law regime. Second, the maximum Lyapunov exponent is large for small viscosity parameter η, i.e., $\lambda_1 \propto \eta^{-1/2}$ in shell models [28], in contrast to a near zero value in our model.

It is also interesting to note that in our model, propagating solutions arise in the power-law regime of stress, which comes as a surprise. As far as we are aware, this is the first situation, both from an experimental and theoretical angle, where propagating solutions are seen in a marginally stable situation.

Regarding the band types seen in the model, we stress that these features emerge purely due to dynamical reasons without any recourse to using the negative strain rate sensitivity feature as an input, as is the case in most models [48,53–55]. Even the recently introduced polycrystalline plasticity model, which reproduces the crossover behavior, also uses the negative strain rate sensitivity as an input [56]. Further, the dynamical approach followed here clearly exposes how the slowing down of the plastic relaxation occurs *due to a feedback mechanism of dislocation multiplication and ap-*

plied strain rate as we reach the power-law regime of stress drops. While the three different types of bands have features of the uncorrelated type *C*, hopping type *B*, and the propagating type *A* bands found in polycrystalline materials, there is no element of polycrystallinity in the model in its present form. In polycrystals, other types of coupling terms do arise, which are also modeled by diffusive-type terms [1]. One way of including the effect of grain boundaries within the natural setting of the model is to recognize that cross slip will be hindered near the grain boundaries. This also leads to a term similar to the diffusive term, which can account for the back stress arising from the incompatibility of grains. As the form of these terms are similar, the basic results are unlikely to change, although one should expect a competition between the terms operating within a crystal and that at the grain boundaries.

From a purely dynamical point of view, this model should be of interest to the area of dynamical systems, as it appears to be fully dynamical model that exhibits a crossover from a chaotic to a power-law regime, in the sense that our model is continuous space-time model *without any recourse to artificial thresholds* as is done in coupled map lattices [57]. We note also that while the slow manifold subspace gives a method of visualizing the dislocations configurations, particularly in the scaling regime, the complementary subspace of the fast variable has helped us to obtain the band velocity in the same regime of strain rates. From the point of view of plastic instabilities, the present dynamical approach should be a promising direction for explaining many other patterns mentioned in the Introduction [1].

Finally, as stated earlier, the PLC effect bears considerable similarity with many stick-slip systems and hence presents a way of understanding some of these systems. Here, we comment on the similarity of the model for a possible adoption to the observed voltage fluctuations in charge-density wave compounds [12]. Under the action of applied electric field, anomalously large voltage fluctuations are reported when the electric field is above the threshold value. This ohmic-to-nonohmic transition in $K_{0.3}MoO_3$ and $Rb_{0.3}MoO_3$, for instance [58], has not been adequately explained, although the similarity with the PLC effect has been noted [12]. Lee and Rice [59] have suggested that phase dislocations of the charge-density waves carry current at fields too low for the charge-density waves to move as a whole. Indeed, both fall in the category of the pinning-depinning phenomenon. In the case of charge-density waves, pinned at impurity/defect sites is unpinned due to the applied electric field. The threshold value of the electric field can be viewed as the onset of plastic flow of the charged phase dislocations [12]. These authors identify stress with voltage and strain with current, and suggest that the total current is the sum of the ohmic part and that arising from charge-density waves corresponding to the elastic and plastic displacements in the PLC instability. We believe that this parallel can be taken further along the lines of our PLC model, where one can identify the phase dislocations with mobile dislocations, the neutral defects of the charge-density wave with dislocation dipoles, i.e., the immobile and phase dislocations pinned at defects with the Cottrell type [60]. Work along these lines is in progress.

The results in this paper, as well as those in our recent papers, would not have been possible if not for the fruitful collaboration with Dr. D. Sahoo that resulted in the model in 1981. The senior author (G.A) is grateful for the collaborative effort. This work is supported by Department of Science and Technology, New Delhi, India.

[1] L. P. Kubin, C. Fressengeas, and G. Ananthakrishna, in *Collective Behaviour of Dislocations*, edited by F. R.N. Nabarro and M. S. Deusbery (North-Holland, Amsterdam, 2002), Vol. 11, p. 101.
[2] A detailed study of this effect may be found in F. Le Chatelier, Rev. de Métal. **6**, 914 (1909). However, the phenomenon was first observed by F. Savart [Ann. Chim. Phys., Second series, **65**, 337 (1937)].
[3] M. Zaiser and P. Hähner, Phys. Status Solidi B **199**, 267 (1997).
[4] A. H. Cottrell, *Dislocations and Plastic Flow in Crystals* (Clarendon, Oxford, 1953).
[5] A. Van den Beukel, Phys. Status Solidi A **30**, 197 (1975).
[6] L. P. Kubin and Y. Estrin, Acta Metall. **33**, 397 (1985).
[7] P. Penning, Acta Metall. **20**, 1169 (1972).
[8] J. Weertman, Can. J. Phys. **45**, 797 (1967).
[9] B. N. J. Persson and E. Tosatti, *Physics of Sliding Friction* (Kluwer, Dordrecht, 1996).
[10] J. M. Carlson and J. S. Langer, Phys. Rev. Lett. **62**, 2632 (1989); Phys. Rev. A **40**, 6470 (1989).
[11] D. Maugis and M. Barquins, *Adhesion*, edited by K. W. Allen (Elsevier, London, 1988), Vol. 12.
[12] J. Dumas and D. Feinberg, Europhys. Lett. **2**, 555 (1986).
[13] G. Ananthakrishna and M. C. Valsakumar, J. Phys. D **15**, L171 (1982). The basic model was actually introduced in G. Ananthakrishna and D. Sahoo, J. Phys. D **14**, 2081 (1981).
[14] S. Rajesh and G. Ananthakrishna, Phys. Rev. E **61**, 3664 (2000).
[15] G. Ananthakrishna and M. C. Valsakumar, Phys. Lett. **95**, 69 (1983).
[16] G. Ananthakrishna *et al.*, Scr. Metall. Mater. **32**, 1731 (1995).
[17] S. J. Noronha *et al.*, Int. J. Bifurcation Chaos Appl. Sci. Eng. **7**, 2577 (1997).
[18] A. J. Lichtenberg and M. A. Libermann, *Regular and Chaotic Dyanmics* (Springer-Verlag, New York, 1991).
[19] H. D. I. Abarbanel, *Analysis of Observed Chaotic Data* (Springer-Verlag, New York, 1996).
[20] G. Ananthakrishna *et al.*, Phys. Rev. E **60**, 5455 (1999).
[21] M. S. Bharathi *et al.*, Phys. Rev. Lett. **87**, 165508 (2001).
[22] P. Bak, C. Tang, and K. Wiesenfeld, Phys. Rev. Lett. **59**, 381 (1987); Phys. Rev. A **38**, 364 (1988).
[23] P. Bak, *How Nature Works* (Springer-Verlag, New York, 1996).
[24] H. J. Jensen, *Self-Organized Criticality* (Cambridge University Press, Cambridge, 1998).

[25] G. D'Anna and F. Nori, Phys. Rev. Lett. **85**, 4096 (2000); S. V. Franklin, F. Martens, and M. Marder, Phys. Rev. E **62**, 8195 (2000); Phys. Rev. Lett. **78**, 4502 (1997).
[26] See, for instance, F. Heslot, B. Castaing, and A. Libchaber, Phys. Rev. A **36**, 5870 (1987).
[27] T. Bohr, M. H. Jensen, G. Paladin, and A. Vulpiani, *Dynamical Systems Approach to Turbulence* (Cambridge University Press, Cambridge, England, 1997).
[28] M. Yamada and K. Ohkitani, J. Phys. Soc. Jpn. **56**, 4210 (1987); M. Yamada and K. Ohkitani, Phys. Rev. Lett. **60**, 983 (1988); Prog. Theor. Phys. **79**, 1265 (1988);A. Cristani *et al.*, Physica D **76**, 239 (1994), and the references therein.
[29] B. Gutenberg and C. F. Richter, Ann. Geofis. **9**, 1 (1956).
[30] X. Che and H. Suhl, Phys. Rev. Lett. **64**, 1670 (1990); K. L. Babcock and R. M. Westervelt, *ibid.* **64**, 2168 (1990).
[31] M. S. Bharathi and G. Ananthakrishna, Europhys. Lett. **48**, 1355 (2002).
[32] M. S. Bharathi and G. Ananthakrishna, Phys. Rev. E **67**, 065104(R) (2003).
[33] M. Bekele and G. Ananthakrishna, Phys. Rev. E **56**, 6917 (1997).
[34] S. Rajesh and G. Ananthakrishna, Physica D **140**, 193 (2000).
[35] M. V. Glazov *et al.*, Appl. Phys. A: Mater. Sci. Process. **64**, 373 (1997).
[36] M. Zaiser *et al.*, Comput. Mater. Sci. **5**, 35 (1999).
[37] There are a number of simplifications used in the model. For instance, we have used only quadratic and biquadratic nonlinearities, an obvious simplification of realistic terms like $\rho_{im}^{1/2}\rho_m$, but an essential one for analytical work (see, for instance, [14,33,34]). It is also possible to introduce additional variables, for instance, the density of solute atoms stored in the Cottrell-type of dislocations. However, these additional terms tend only to obscure the physics of the PLC effect. In this sense, the model should be regraded as some kind of minimal model.
[38] A. Milik *et al.*, Int. J. Bifurcation Chaos Appl. Sci. Eng. **8**, 505 (1998).
[39] N. H. Packard, J. P. Crutchfield, J. D. Farmer, and R. S. Shaw, Phys. Rev. Lett. **45**, 712 (1980).
[40] P. Grassberger and I. Procaccia, Physica D **9**, 189 (1983).
[41] M. Ding, C. Grebogi, E. Ott, T. Sauer, and J. A Yorke, Phys. Rev. Lett. **70**, 3872 (1993).
[42] D. Broomhead and G. King, Physica D **20**, 217 (1987).
[43] G. Benettin, L. Galgani, A. Giorgilli, and J. M. Strelcyn, Mechanica **15**, 9 (1980).
[44] D. Ruelle, Commun. Math. Phys. **87**, 287 (1982).
[45] M. S. Bharathi, S. Rajesh, and G. Ananthakrishna, Scr. Mater. **48**, 1355 (2003).
[46] G. Dee and J. S. Langer, Phys. Rev. Lett. **50**, 383 (1983).
[47] W. van Saarloos, Phys. Rev. A **37**, 211 (1988).
[48] P. Hähner, A. Ziegenbein, E. Rizzi, and H. Neuhäuser, Phys. Rev. B **65**, 134109 (2002).
[49] A. Korbel, J. Zasadzinski, and Z. Siekluka, Acta Metall. **24**, 921 (1976).
[50] A. Erzan and S. Sinha, Phys. Rev. Lett. **66**, 2750 (1991).
[51] M. de Sousa Vieira and A. J. Lichtenberg, Phys. Rev. E **53**, 1441 (1996).
[52] B. Cessac, Ph. Blanchard, and T. Kruger, Phys. Rev. E **64**, 016133 (2001).
[53] P. G. McCormick and C. P. Ling, Acta Metall. Mater. **43**, 1069 (1995).
[54] S. Zhang, P. G. McCormick, and Y. Estrin, Acta Mater. **49**, 1087 (2001).
[55] M. Lebyodkin, L. Dunin-Barkowskii, Y. Bréchet, Y. Estrin, and L. P. Kubin, Acta Mater. **48**, 2529 (2000), and the references therein.
[56] S. Kok, M. S. Bharathi, A. J. Beaudoin, C. Fressengeas, G. Ananthakrishna, L. P. Kubin, and M. Lybyodkin, Acta Mater. **51**, 3651 (2003).
[57] H. Chate and P. Manneville, Physica D **32**, 409 (1988); S. Sinha and D. Biswas, Phys. Rev. Lett. **71**, 2010 (1993); S. Sinha, Int. J. Mod. Phys. B **9**, 875 (1994); T. Bohr *et al.*, Phys. Rev. Lett. **86**, 5482 (2001).
[58] J. Dumas, C. Schlenker, J. Marcus, and R. Buder, Phys. Rev. Lett. **50**, 757 (1983); J. Dumas and C. Schlenker, Lect. Notes Phys. **217**, 439 (1985).
[59] P. A. Lee and T. M. Rice, Phys. Rev. B **19**, 3970 (1979).
[60] G. Ananthakrishna, J. Indian Inst. **78**, 165 (1998).